Journal of Physics: Conference Series

PAPER • **OPEN ACCESS**

Coherent structures in turbulent boundary layers over an airfoil

To cite this article: Marco Atzori *et al* 2020 *J. Phys.: Conf. Ser.* **1522** 012020

View the article online for updates and enhancements.

You may also like

- Coherent structures in a zero-pressure-gradient and a strongly decelerated boundary layer
Mark P Simens, Ayse G Gungor and Yvan Maciel
- Large-eddy simulations of adverse pressure gradient turbulent boundary layers
Alexandra Bobke, Ricardo Vinuesa, Ramis Örlü et al.
- Detection of coherent structures in a turbulent boundary layer with zero, favourable and adverse pressure gradients
A Drozdz and W Elsner

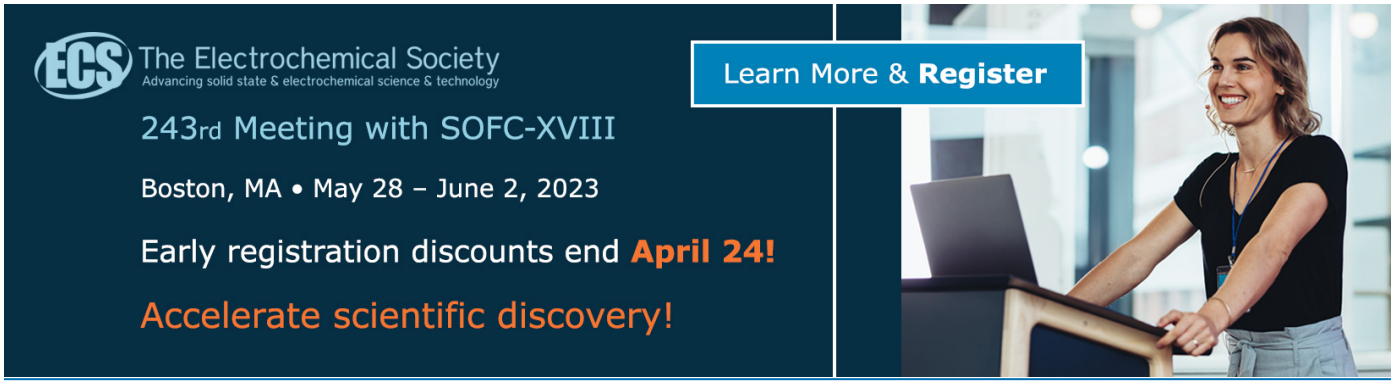

This content was downloaded from IP address 131.175.148.48 on 14/03/2023 at 14:07

Coherent structures in turbulent boundary layers over an airfoil

Marco Atzori[a], Ricardo Vinuesa[a], Adrián Lozano-Durán[b] and Philipp Schlatter[a]

[a] Linné FLOW Centre, KTH Mechanics, SE-100 44 Stockholm, Sweden and Swedish e-Science Research Centre (SeRC), Stockholm, Sweden
[b] Center for Turbulence Research, Stanford, CA, USA

E-mail: atzori@mech.kth.se

Abstract. This preliminary study is concerned with the identification of three-dimensional coherent structures, defined as intense Reynolds-stress events, in the turbulent boundary layer developing over the suction side of a NACA4412 airfoil at a Reynolds number based on the chord lenght and the incoming velocity of $Re_c = 200,000$. The scientific interest for such flows originates from the non-uniform adverse pressure gradient that affects the boundary-layer development. Firstly, we assess different methods to identify the turbulent-non-turbulent interface, in order to exclude the irrotational region from the analysis. Secondly, we evaluate the contribution of the considered coherent structures to the enhanced wall-normal velocity, characteristic of adverse pressure gradients. Our results show that it is necessary to limit the detection of coherent structures to the turbulent region of the domain, and that the structures reveal qualitative differences between the contributions of intense events to the wall-normal velocity in adverse-pressure-gradient and zero-pressure-gradient turbulent boundary layers.

1. Introduction

Turbulent boundary layers (TBLs) subjected to pressure gradients have been widely studied, both experimentally and via numerical simulations. High-fidelity numerical simulations were first employed to investigate adverse-pressure-gradient (APG) effects on flat-plate turbulent boundary layers by Spalart and Watmuff [1]. Some of the pioneering numerical studies on the flow around wing profiles include the large-eddy simulation (LES) performed by Jansen [2] (NACA4412) and the direct numerical simulation (DNS) performed by Shan *et al.* [3] (NACA0012), which was limited to $Re_c = 100,000$. Note that the Reynolds number is defined as $Re_c = U_\infty c/\nu$, where U_∞ is the incoming velocity, c the chord length of the airfoil, and ν the kinematic viscosity. Our group has performed a DNS of the flow around a NACA4412 at $Re_c = 400,000$, which is the highest Reynolds number for a DNS on such cases studied so far [4], and a series of well-resolved LES at Re_c up to $1,000,000$ [5].

As discussed by Bobke *et al.* [6], to explain the behaviour of turbulent boundary layers subjected to pressure gradients it is necessary to consider the combined effects of the Reynolds number and the spatial development of the Clauser pressure-gradient parameter β. Note that the Clauser pressure-gradient parameter is defined as $\beta = \delta^*/\tau_w \, \mathrm{d}P_e/\mathrm{d}x_t$, where δ^* is the displacement thickness, τ_w is the mean wall-shear stress and $\mathrm{d}P_e/\mathrm{d}x_t$ is the derivative of the pressure at the boundary-layer edge in the wall-parallel direction. How the Reynolds number and

Content from this work may be used under the terms of the Creative Commons Attribution 3.0 licence. Any further distribution of this work must maintain attribution to the author(s) and the title of the work, journal citation and DOI.
Published under licence by IOP Publishing Ltd

the streamwise pressure distribution interact in determining the state of the turbulent boundary layer in complex cases, such as the flow around wings, is still an open question. Besides the traditional approach of considering the statistical properties of the flow, several recent studies have focused on the characterisation of so-called coherent structures, *i.e.* regions of the domain which exhibit a certain degree of homogeneity in space. An example of such structures are the intense Reynolds-stress events, firstly recognised to play a relevant role in the dynamics of the flow by Wallace *et al.* [7]. Lozano-Durán *et al.* [8] characterised these events in turbulent channel flow, and Maciel *et al.* [9] studied the same structures in TBLs subjected to weak and strong APGs. They found that the instantaneous structures are significantly affected by the presence of the pressure gradient and, in particular, they reported that in stronger APGs wall-attached structures are less common, they tend to be more elongated in the spanwise direction rather than in the streamwise and that their spatial organisation is more chaotic. Some of these observations have been confirmed by Tanarro *et al.* [10] through analysis of power-spectral-density distributions around wings.

In the present paper, we consider the three-dimensional Reynolds-stress coherent structures already examined by Lozano-Durán *et al.* [8] and Maciel *et al.* [9] and we study the TBL developing over the suction side of a NACA 4412 wing section at $Re_c = 200,000$. To identify the effects of the non-uniform pressure gradient, we perform a comparison with the zero-pressure-gradient (ZPG) TBL data-set described in Ref. [11], with Reynolds numbers based on the momentum thickness between $Re_\theta = 620$ and $Re_\theta = 2140$. The procedure described in Ref. [8] can be summarised in the following steps: 1) perform the percolation analysis, by means of which it is possible to calibrate the threshold used to identify the structures; 2) identify the considered three-dimensional structures; and 3) compute statistics of the size and location of the structures as well as conditional averages. Contrary to channel flow, the interface between the TBL and the irrotational region requires specific care, and in this study we evaluate how different definitions of the interface can impact the results of the structure identification. Subsequently, we consider the wall-normal velocity conditioned to intense to intense uv events, to investigate how these structures are related with the stronger wall-normal convection characteristic of APG TBLs.

The paper is organized as follows: in section 2, we describe the considered data-sets and the procedure for structure identification; in section 3, we present the results of the percolation analysis and a preliminary study of the relation between coherent structures and the wall-normal convection in APG; in section 4, we summarise our results.

2. Methodology

In this section, we describe the APG and ZPG data-sets and the definition of coherent structures, including the different criteria for identifying the turbulent-non-turbulent-interface (TNTI).

2.1. Data-set

The numerical simulation of the wing section was performed with the spectral-element code *Nek5000* [12], using the $P_N - P_{N-2}$ formulation. The numerical domain is decomposed into hexahedral elements, and velocity and pressure are represented inside each element by Lagrangian interpolants defined on nodes with Gauss–Lobatto–Legengre (GLL) and Gauss–Lobatto (GL) distributions, respectively. The domain sizes are $6c$, $4c$ and $0.2c$ in the streamwise, vertical and spanwise directions, respectively, and the leading edge of the airfoil is located at a distance of $2c$ from the inflow. The simulation is a well-resolved LES, based on the relaxation-term filter proposed by Schlatter *et al.* [13]. The resolution within the turbulent boundary layer around the wing profiles is $\Delta x_t^+ = 18$, $\Delta y_n^+ = (0.64, 11)$ and $\Delta z^+ = 9$ in the tangential, wall-normal and spanwise directions, respectively. Using polynomial order of 11^{th}, to reach this resolution required approximately $127,000$ elements and 220 million grid points. The location of transition to turbulence is prescribed by applying tripping at $x/c = 0.1$ on pressure and suction

sides, which is implemented as described by Schlatter and Örlü [14]. We employ a Reynolds-averaged Navier–Stokes (RANS) numerical simulation with the $k-\omega$ SST turbulent model [15] in a much larger computational domain to obtain the velocity distribution at the inflow, upper and lower boundaries of the LES domain, which is imposed in the LES as a Dirichlet boundary condition. The outlet boundary condition is the stabilized outflow proposed by Dong *et al.* [16], and the boundary conditions in the span-wise direction are periodic. We considered a region of the domain that extends above the suction side of the airfoil up to a distance of $0.12c$ in the wall-normal direction, performing the identification of turbulent structures only in the turbulent portion of the flow, as discussed later on. The structure identification is also limited in the streamwise direction between $x/c = 0.2$ and $x/c = 0.9$ to avoid both transitional (low-Re) and extreme pressure-gradient effects, as illustrated in Fig. 1. The wing data-set consists of approximately 160 independent velocity fields.

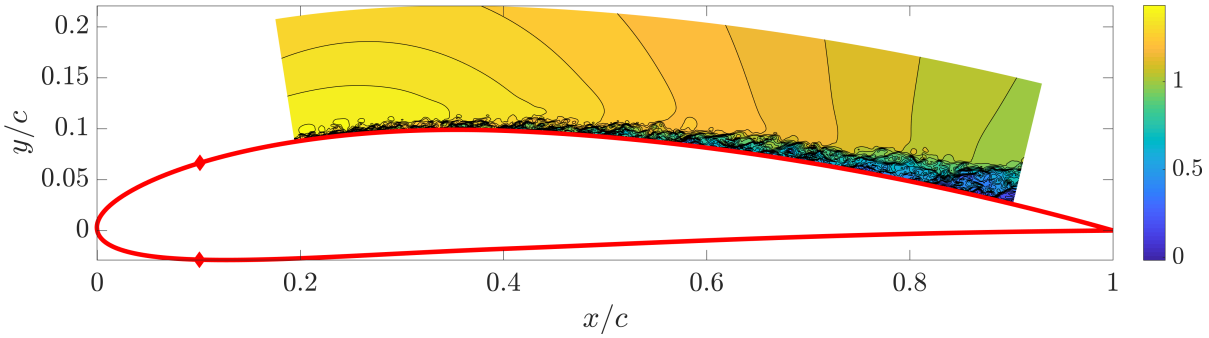

Figure 1. Contour plot of the horizontal component of the velocity in an arbitrary field of the wing data-set, limited to the area where the structure identification is performed. The red line indicates the airfoil surface and the red diamonds the tripping locations.

The ZPG TBL simulation is part of the DNS data-set described by Jiménez *et al.* [11] and it was performed using compact finite differences in the wall-normal and streamwise directions and Fourier decomposition in the spanwise (periodic) direction. The code is described in detail in Ref. [17]. The computational domain is $535\theta \times 29\theta \times 88\theta$, where θ is the momentum thickness at midway into the simulation box, and the resolutions in the three directions are $\Delta x^+ = 6.1$, $\Delta y^+ = 0.3$ and $\Delta z^+ = 4.1$. The ZPG data-set consists of 38 independent velocity fields. We refer to Ref. [18] and Refs. [11, 17] for a more detailed description of the wing and TBL simulations, respectively.

2.2. Coherent structure identification

We focus on coherent structures in turbulent boundary layers defined as connected regions in the domain where the following condition is fulfilled:

$$|uv| > H u_{\rm rms} v_{\rm rms}\,, \tag{1}$$

with u and v being the fluctuations of the wall-tangential and wall-normal components of the velocity with respect to the mean, $u_{\rm rms}$ and $v_{\rm rms}$ are their root-mean-squared values and H is a non-dimensional threshold value. In the following, we use the superscript $\tilde{}$ to indicate instantaneous values, capital letters for the time average and lowercase letters for the fluctuations, so that the Reynolds decomposition for the tangential velocity is written as: $\tilde{u}(t) = U + u(t)$. Expression (1) is equivalent to that proposed by Wallace [7] to perform the quadrant analysis, and employed by Lozano-Durán *et al.* [8] in turbulent channel flow. Although Maciel *et al.* [9] reported that they applied the same technique in APG TBL directly as done

in Ref. [8], we note that condition (1) may give unexpected results in TBL when used together with the classical Reynolds decomposition to define the velocity fluctuations. This is because velocity fluctuations are not only present in the turbulent region of the boundary layer, but they may extend even further out beyond the TNTI. In fact, Kwon *et al.* [19] pointed out the necessity of considering the TNTI in computing the mean velocity and Hwang and Sung [20], who studied structures of velocity fluctuations, took this aspect into account.

To assess the possible impact of not considering the TNTI in the identification of the structures, we applied condition (1), making use of the standard Reynolds decomposition, coupled with an additional condition to discriminate between turbulent and non-turbulent regions. Different definitions of the TNTI interface have been formulated, which can be equivalent in a mean sense, but it is not obvious what effect these may have on the properties of the coherent structures in the proximity of the interface. Therefore, we compare three different criteria: the first criterion is that proposed by Bisset *et al.* [21], and it is based on the enstrophy (*i.e.* the module of the instantaneous vorticity), defined as:

$$|\tilde{\omega}| = \sqrt{\tilde{\omega}_x^2 + \tilde{\omega}_y^2 + \tilde{\omega}_z^2}\,. \tag{2}$$

Note that x and y are coordinates tangential and normal to the wall, respectively. Turbulent regions are defined as the volumes where $|\tilde{\omega}|$, normalised by the mean velocity at the boundary-layer edge (U_e) and the 99% boundary-layer thickness (δ_{99}^D), is higher than a threshold C_ω, *i.e.* if $|\tilde{\omega}| > C_\omega U_e \delta_{99}^D$. The second criterion was proposed by Chauhan *et al.* [22] and was originally applied to experimental data. It defines the turbulent boundary layer as the region where a modified instantaneous turbulent kinetic energy, $\tilde{k}^*$, is higher than a certain value characterising the turbulence intensity in the free stream. The condition is expressed as: $\tilde{k}^* > C_k^f U_\infty^2/2$, where C_k^f is a numerical threshold and U_∞ is the free-stream velocity. In the original formulation of this criterion, the variable $\tilde{k}^*$ is the instantaneous kinetic energy computed in a frame of reference moving with the incoming fluid velocity and averaged over a box of volume $\mathcal{V}^*$:

$$\tilde{k}^* = \frac{1}{\mathcal{V}^*} \int \left(\frac{1}{2}(\tilde{u} - U_\infty)^2 + \tilde{v}^2 + \tilde{w}^2 \right) \mathrm{d}\mathcal{V}^*\,, \tag{3}$$

We modified the definition of $\tilde{k}^*$ to take into account the relatively strong wall-normal convection induced by the adverse pressure gradient in the proximity of the trailing edge of the airfoil, using:

$$\tilde{k}^* = \frac{1}{\mathcal{V}^*} \int \left((\tilde{u} - U_e)^2 + (\tilde{v} - V_e)^2 + \tilde{w}^2 \right) \mathrm{d}\mathcal{V}^*\,, \tag{4}$$

where V_e is the wall-normal velocity at the boundary-layer edge. With such a modification, the mean wall-normal distance of the TNTI, δ_I, matches the boundary-layer thickness δ_{99}^D for a given C_k^f, while the original definition led to progressively higher difference between the mean δ_{99}^D and δ_I farther downstream, when V_e is higher. Note that the volume average included in condition (4), motivated by the measurement noise in the original formulation, improves the method, in particular for the APG data-set (*i.e.* the resulting average δ_I has a better agreement with δ_{99}). Lastly, we introduce a third criterion, defining the turbulent region of the domain as the volume where the instantaneous turbulent kinetic energy, computed as:

$$\tilde{k} = \frac{1}{2}(u^2 + v^2 + w^2)\,, \tag{5}$$

is higher than a certain fraction of the turbulent kinetic energy at the boundary-layer edge, computed as

$$k_e = \frac{1}{2}(\overline{u_e^2} + \overline{v_e^2} + \overline{w_e^2})\,, \tag{6}$$

where the overbar denotes the time and spanwise average and the subscript e that the quantities are evaluated at $y = \delta_{99}^D$. The corresponding condition is expressed as $\tilde{k} > C_k^e k_e$, where C_k^e is a constant scalar value. The third criterion is motivated by practical considerations, as it can be employed without computing the vorticity or the volume average required, respectively, by the first and the second criteria. Although these operations are simple from a conceptual point of view, their cost in terms of memory requirement or computational time can become significant when processing a large data-set. A possible drawback of condition (6) is a higher sensitivity to δ_{99}, due to the fact that k exhibits a stronger variation than the mean velocity in the interface region.

All the considered criteria require the selection of a value for the numerical parameters C_ω, C_k^* and C_k, and the identification of the boundary-layer edge to compute the corresponding scaling factors U_e/δ_{99}^D, U_e^2 and k_e. We estimate the location of the boundary-layer edge using the concept of the diagnostic plot [23], as proposed by Vinuesa *et al.* [24]. This procedure takes advantage of the collapse of the curve $u_{\mathrm{rms}}/(U\sqrt{H_{12}})$ as a function of U/U_e, defining the boundary-layer edge in terms of the value of the local turbulence intensity that corresponds to $U/U_e = 0.99$. Note that H_{12} is the shape factor, defined as δ^*/θ. Vinuesa *et al.* [24] showed that this technique gives results in good agreement with both the composite profiles methods proposed by Chauhan *et al.* [25] and Nickels [26]. Given the estimate of δ_{99}^D, we set the parameters $C_\omega = 0.1$, $C_k^f = 0.0075$ and $C_k^e = 0.6$ so that the mean wall-normal distance of the TNTI is equivalent to the boundary-layer thickness δ_{99}^D. Fig. 2 illustrates the wall-normal location of the

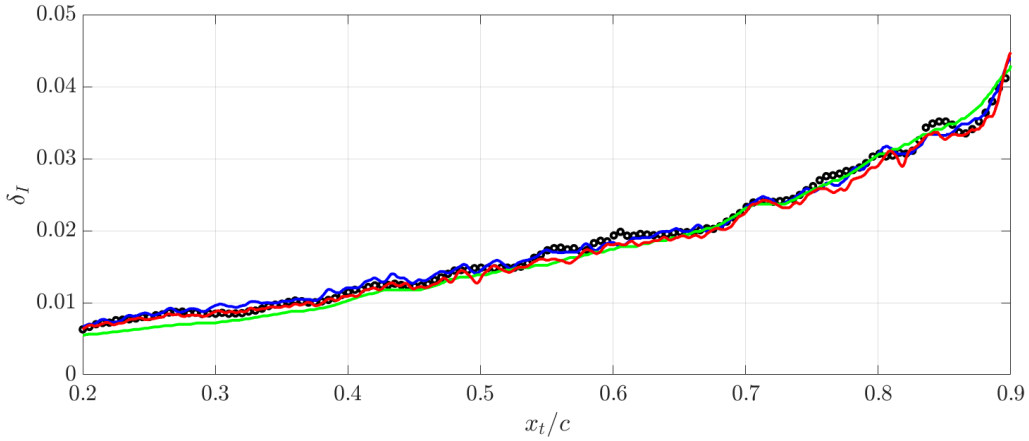

Figure 2. Comparison between the mean wall-normal location of the TNTI for different criteria, averaged over the spanwise direction of a single flow field of the APG data-set. Solid blue, green and red lines for $|\tilde{\omega}| > C_\omega U_e/\delta_{99}^D$, $\tilde{k}^* > C_k^f U_\infty^2/2$, and $\tilde{k} > C_k^e k_e$, respectively, with $C_\omega = 0.1$, $C_k^f = 0.0075$ and $C_k^e = 0.6$. The black circles are δ_{99}^D estimated with the diagnostic scaling.

TNTI estimated using the three criteria and averaged over the spanwise direction of a single field of the wing data-set, compared with δ_{99}^D calculated using the diagnostic scaling based on U and u_{rms} averaged over the same field. The good agreement between the four curves shows that all the considered criteria, although not exactly equivalent, follow the streamwise development of the turbulent boundary layer both quantitatively and qualitatively.

3. Results

In this section, we assess the impact of considering the TNTI in the identification of turbulent structures, and the results of average and fractional contribution of the wall-normal velocity

component conditioned on intense uv events.

3.1. Impact of the TNTI on the percolation analysis

To qualitatively assess the effect of taking into account the wall-normal location of the TNTI interface in the identification of structures, we compare the turbulent region of the domain according to the three criteria discussed above and the connected components fulfilling condition (1). Fig. 3 shows the wall-tangential instantaneous velocity component on the frontal section at $x/c = 0.8$ of an arbitrary field of the wing data-set, and the location of the TNTI according to the three criteria in the same section. In this figure we also show the regions of the domain where $|uv| > H u_{\rm rms} v_{\rm rms}$ for $H = 0.5$ and $H = 2.0$, which are values lower and higher than that of the percolation crisis, respectively. For each criterion, we define the TNTI at each spanwise location as the point farthest from the wall where the condition is fulfilled. The three TNTIs are qualitatively similar, although they differ in specific locations. In addition, the criteria differ in the region below the TNTI. The first criterion, based on the enstrophy, excludes the sparse irrotational spots in the turbulent boundary layer, which are occasionally part of intense Reynolds-stress structures. On the other hand, the second criterion includes in the turbulent region almost the entire portion of the domain below the TNTI. The third criterion, based on the instantaneous turbulent kinetic energy, excludes the spots where the turbulent flow is similar to the mean flow. However, in the example considered here, all the regions identified as intense Reynolds-stress events and below the TNTI, are also included in the turbulent region, as determined by the third criterion. The third criterion also excludes a thin layer close to the wall, approximately corresponding to the viscous sublayer. This fact is not considered a drawback, as the viscous sublayer is usually excluded a priori during the identification of turbulent structures in internal flows, such as duct and channel [27].

Remarkably, it is apparent that using condition (1) alone is not enough to distinguish turbulent structures from fluctuations in the non-turbulent region of the domain, because the identified connected components can extend across the TNTI and well above $y_n = \delta_{99}^D$. This fact needs to be taken into account because the fluctuations in the non-turbulent region occupy a relatively large volume if compared with intense Reynolds-stress events, and it has an impact on the percolation analysis, as discussed below.

Moisy and Jiménez [28] observed that a percolation crisis occurs in isotropic turbulence for dissipative structures as well as for vortex clusters. Lozano-Durán *et al.* [8] performed the percolation analysis for intense Reynolds-stress events in channel flow, to describe the effects of changing the values of the numerical threshold H. This analysis consists of examining the ratio of the volume of the largest structure and the total volume occupied by all the structures, $\mathcal{V}_{\rm max}/\mathcal{V}_{\rm all}$, as a function of H, and it is used in the present context to asses whether the identification of the structures is affected by the inhomogeneity of the flow in the wall-normal and streamwise direction. If the probability of belonging to coherent structures is homogeneous in the domain a percolation crisis occurs at an intermediate value of the threshold H. For low values of H, $\mathcal{V}_{\rm max}/\mathcal{V}_{\rm all} \approx 1$, when few and large connected components occupy most of the volume, and for high values of H, $\mathcal{V}_{\rm max}/\mathcal{V}_{\rm all} \approx 0$, when the structures are relatively numerous and small. The percolation crisis consists of a relatively sharp transition between the two limits of low and high H, when small structures substitute the larger ones. For an infinitely extended domain, the connectivity of the system determines the slope of the percolation curve in the proximity of the crisis [29], whereas, in the case of finite size, the percolation curve will also depend on the specific realisation of the considered variables. In the present context, see for instance Refs. [28, 8], the averaged percolation curve over multiple fields is often considered. This operation is appropriate if the domain size is large enough to have no direct impact on the results, *i.e.* if the typical correlation length of the data-set is short enough.

In Fig. 4, we compare the results of the percolation analysis on the APG TBL over the

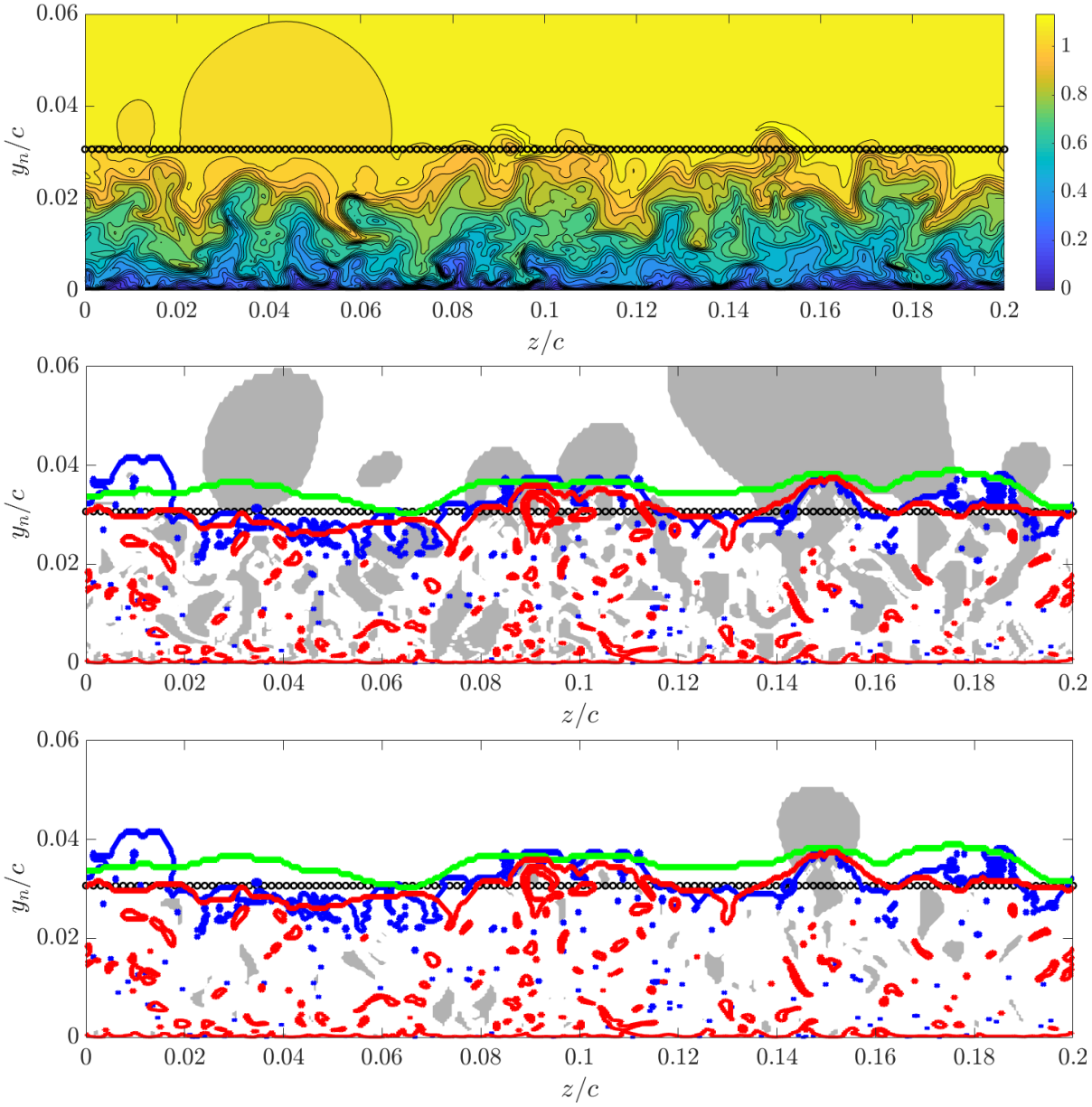

Figure 3. (Top) Contour plot of the instantaneous streamwise velocity for an arbitrary field of the wing data-set, at the streamwise location $x/c = 0.8$, and (centre and bottom) comparison between the turbulent region of the domain according to the three considered definitions of the TNTI and intense Reynolds-stress structures at the same location. The grey contours indicate the region of the domain where $|uv| > Hu_{\mathrm{rms}}v_{\mathrm{rms}}$, for (centre) $H = 0.5$ and (bottom) $H = 2.0$. The colour code for blue, green, red and the black circles is the same as in Fig. 2.

suction side of the NACA4412 airfoil and on the ZPG TBL data-set with that of channel flow at a friction Reynolds number of 180 [27]). Note that $Re_\tau = hu_\tau/\nu$, where h is the half height of the channel and u_τ is the friction velocity. We performed the percolation analysis both

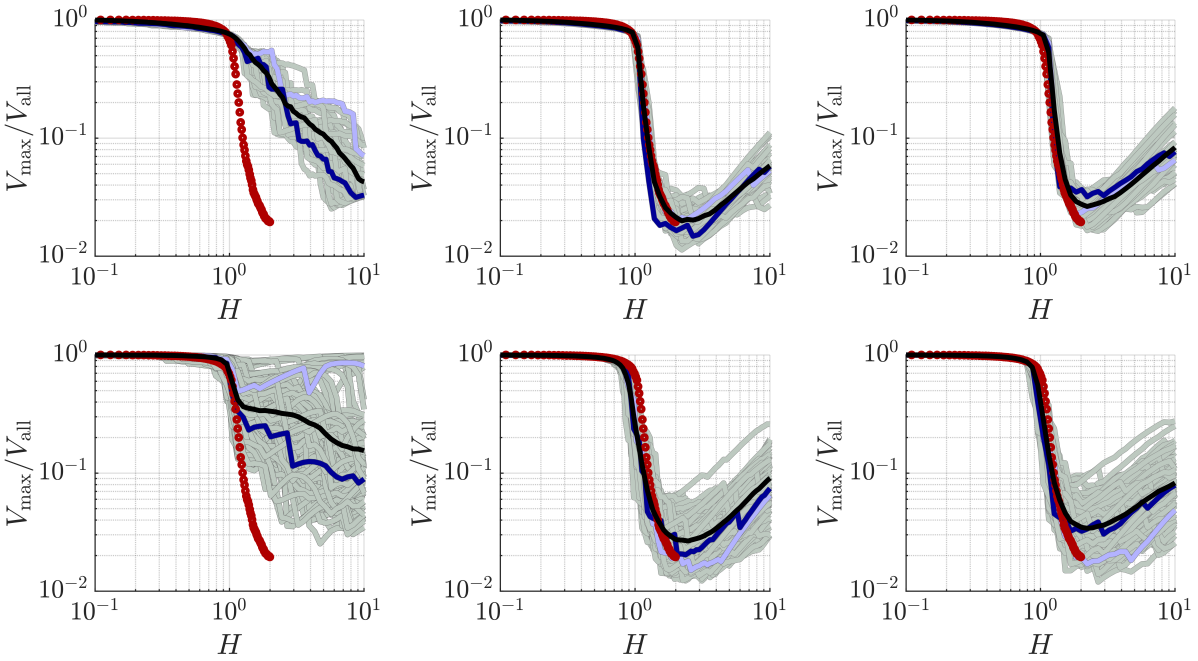

Figure 4. Comparison between the percolation analysis for (top) ZPG and (bottom) APG, considering three different conditions for structure identification: (left column) $|uv| > Hu_{\text{rms}}v_{\text{rms}}$, (centre column) $|uv| > Hu_{\text{rms}}v_{\text{rms}}$ and $\tilde{k}^* > C_k^f U_\infty^2$, and (right column) $|uv| > Hu_{\text{rms}}v_{\text{rms}}$ and $\tilde{k} > C_k^e k_e$, for $C_k^f = 0.0025$ and $C_k^e = 0.6$. The solid grey lines are the ratio between the volume of the largest structure, $\mathcal{V}_{\max}$, and the total volume occupied by structures, $\mathcal{V}_{\text{all}}$, for every field in the data-set. The dark and light blue lines are two arbitrarly selected flow fields. The solid black lines are the average $\mathcal{V}_{\max}/\mathcal{V}_{\text{all}}$ over the entire data-set. The red symbols are the results of the percolation for channel flow at $Re_\tau = 180$ [27].

without taking into account the TNTI and using the three criteria previously introduced, and we show the percolation curves for every single field as well as the average to provide additional information. The results for the enstrophy criterion are not shown here, as they are very similar to those of the other two criteria. We first observed that ignoring the TNTI has a significant impact on the results. In the ZPG, the averaged percolation curve has a lower slope, indicating a less evident percolation crisis. For instance, at the threshold value of $H = 2.0$, $\mathcal{V}_{\max} \approx 30\%\mathcal{V}_{\text{all}}$, compared to $\mathcal{V}_{\max} \approx 2\%\mathcal{V}_{\text{all}}$ in the channel at the same H. However, if the coherent structure identification considers only the turbulent region of the domain, the percolation crisis is clearly evident, and the averaged curves for both ZPG and channel are in very good agreement.

The effects of not taking into account the TNTI are even more pronounced in the APG data-set. For certain instantaneous fields, $\mathcal{V}_{\max}/\mathcal{V}_{\text{all}}$ decreases for increasing H, and it exhibits a trend similar to that of the ZPG with the same detection procedure. In other cases, few very large structures can retain a remarkable portion of $\mathcal{V}_{\text{all}}$ up to high values of H. The dark blue and light blue lines in Fig. 4 are examples of the former and latter scenario, respectively. As a consequence of the appearance of these two different behaviours, the averaged percolation curve exhibits a peculiar shape. In fact, although an incipient percolation crisis appears at $H \simeq 1$,

$V_{\max}/V_{\text{all}}$ shows signs of an asymptote towards 0.35 for increasing H. Such a behaviour is not representative of the typical percolation curve for the individual snapshots, and it is instead the consequence of the relative occurrence of the two different trends described above. However, as for the ZPG, taking into account the existence of the TNTI leads to good agreement with channel flow. The differences between the percolation curves of the ZPG and the APG data-sets when the TNTI is ignored are probably related to the difference in the flow and the domain size. We studied this effect progressively reducing the domain size in the ZPG data-set, and we observed that it can have an impact on the percolation curve (results not shown here). This phenomenon is due to the size of regions of fluctuations above the TNTI, which are much larger than the turbulent structures for high values of the threshold H. We did not further investigate this phenomenon, since we will always consider the TNTI definition in the following.

We note that Maciel *et al.* [9], who also considered intense uv events in a similar data-set, did not apply any additional condition related to the location of the TNTI. However, the percolation diagram reported in their work was computed for the quadrants separately, instead of for the entire domain. Since the four quadrants are defined based on the signs of the vertical and horizontal velocity fluctuations, considering them separately means preventing the appearance of large structures at low H. In fact, at such low values of H, $\mathcal{V}_{\max}/\mathcal{V}_{\text{all}}$ is around 0.1, and the maximum value of $\mathcal{V}_{\max}/\mathcal{V}_{\text{all}}$ is reached at the highest values of H, after the percolation crisis. These authors also considered the number of objects as a function of H, normalized with the highest number of objects detected at any H, a quantity denoted by $N/N_{\max}$. As the number of coherent structures identified in the non-turbulent region of the domain is much lower than that in the turbulent region, $N/N_{\max}$ is not affected by the larger structures in the non-turbulent region. Based on the behaviour of this quantity as a function of H, they selected a threshold similar to that employed by Lozano-Durán in channel flow, *i.e.* $H = 1.75$, which is also reasonable in the light of our findings.

The results presented so far suggest that it is adequate to include the definition of the TNTI in the condition employed for turbulent structure identification. However, the percolation analysis does not provide decisive arguments in favour of or against any of the three criteria considered here, which provide very similar percolation curves. In the present study, we will employ the third criterion, which is easiest to implement. Therefore, we consider as coherent structures the regions of the domain that fulfill the conditions:

$$\begin{cases} |uv| > H u_{\text{rms}} v_{\text{rms}} \,, \; H = 2.0 \\ \tilde{k} > C_k^e k_e \,, \; C_k^e = 0.6 \end{cases} , \tag{7}$$

where the instantaneous turbulent kinetic energy $\tilde{k}$ and the turbulent kinetic energy at the edge of the turbulent boundary layer k_e are defined in expressions (5) and (6), respectively.

3.2. Conditional average and fractional contribution

One of the characteristics of APG TBLs is the intense mean wall-normal convection, which is stronger than in the ZPG case. This phenomenon is linked with the other effects of APG, such as the higher inner-scaled mean wall-tangential velocity in the wake region, and the emergence of an outer peak in the turbulent fluctuations. To describe the contribution of the intense Reynolds-stress structures to the wall-normal convection, we consider two different perspectives: firstly, we classify the structures according to the quadrant analysis, and we examine the conditional average of the wall-normal velocity component. The conditional average is computed as:

$$V = \frac{1}{\mathcal{V}_{\text{Q}}} \sum_{i=1}^{N} \mathcal{V}_i \, \tilde{v}_i \Phi_i \,, \quad \text{where} \quad \mathcal{V}_{\text{Q}} = \sum_{i=1}^{N} \mathcal{V}_i \Phi_i \,, \tag{8}$$

where the index i represents grid points of the domain, $\mathcal{V}_i$ is a characteristic volume assigned to each grid point ($\mathcal{V}_i = \Delta x_i \Delta y_i \Delta z_i$), $\tilde{v}$ is the instantaneous wall-normal velocity component, and Φ_i is 1 or 0 if the ith-grid point fulfils both conditions in (7) and belongs to the considered quadrant. We defined the quadrants as in Ref. [7], based on the sign of the fluctuations of the velocity components, so that Q1 events correspond to regions of the domain where $v > 0$ and $u > 0$ (outward interactions), in Q2, $v > 0$ and $u < 0$ (ejections), in Q3, $v < 0$ and $u < 0$ (inward interactions), and in Q4, $v < 0$ and $u > 0$ (sweeps). We choose to perform the analysis for $H = 2.0$, which is just above the percolation crisis, ensuring that the intense events are isolated. Fig. 5 (left) shows the inner-scaled V and the conditional average for the different quadrants for both APG and ZPG. For the APG data-set, we examine the vertical profile at

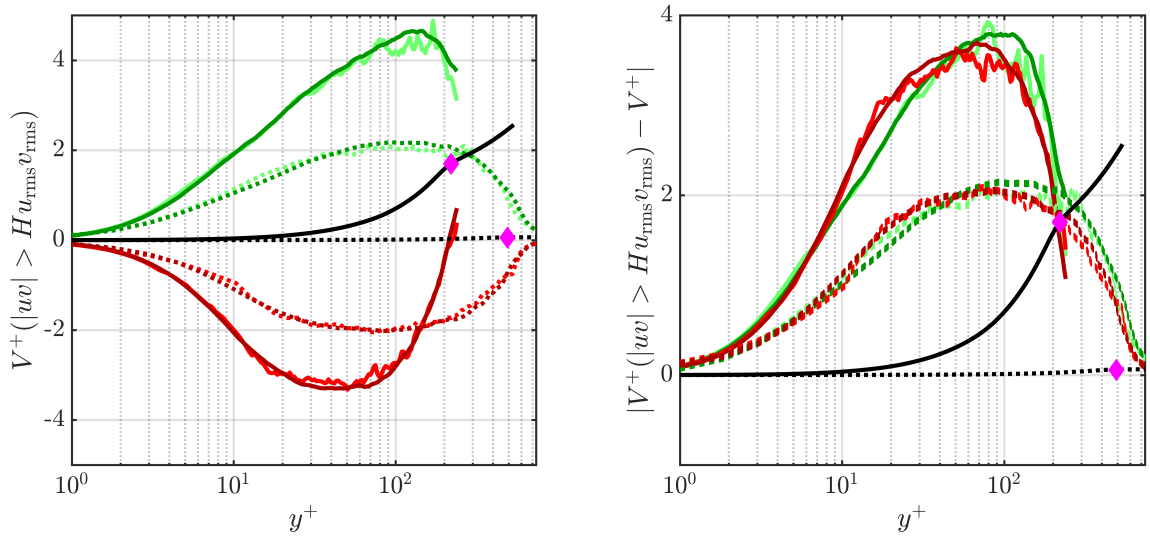

Figure 5. (Left) Inner-scaled conditional average of the wall-normal velocity component over intense uv and (right) absolute value of the same quantity minus the mean V^+, for (solid lines) APG and (dotted lines) ZPG. The average computed over different quadrants is indicated in different colours: light green, dark green, light red and dark red for Q1, Q2, Q3, and Q4, respectively. The black lines are the time average and spanwise. The magenta diamonds indicate the locations of δ_{99}^D.

the streamwise location $x/c = 0.8$, where the friction Reynolds number is $Re_\tau = 226$, and the Reynolds number based on the momentum thickness is $Re_\theta = 1124$. For the ZPG we consider a location where $Re_\tau = 499$ and $Re_\theta = 1200$. Here, the friction Reynolds number is defined as $Re_\tau = u_\tau \delta_{99}^D/\nu$, where u_τ is the friction velocity. Note that the relatively higher Re_θ for the APG data-set is a consequence of the larger boundary-layer thickness, which is a pressure-gradient effect. Interestingly, the conditional average of V is in very good agreement for Q1 and Q2, and for Q3 and Q4, although ejections and sweeps are more common than inner and outward interactions, for both APG and ZPG. Nevertheless, the two cases exhibit qualitative and quantitatively differences. Despite the fact that the same H was employed in both, the module of V is higher for intense events in APG than in ZPG. Such a difference, however, is not as dramatic as the difference between the mean V over the entire flow. Also, while Q1 and Q2 have the same intensity as Q3 and Q4 in ZPG, it appears that the former ones are stronger than the latter in APG. To better characterise the asymmetry between intense events with positive and negative V in APG, we compare the modules of the average of the fluctuations of V conditioned to these events V (Fig. 5, right). Interestingly, the mean of the fluctuations of

Q1 and Q2, and Q3 and Q4 are in good agreement, similar to what observed in ZPG. This fact implies that the APG affects the intensity of both ejections and sweeps in the same way.

We also investigated the scaling properties of the conditional average of V as a function of the wall-normal distance (Fig. 6). Due to the continuity equation and the fact that U and W

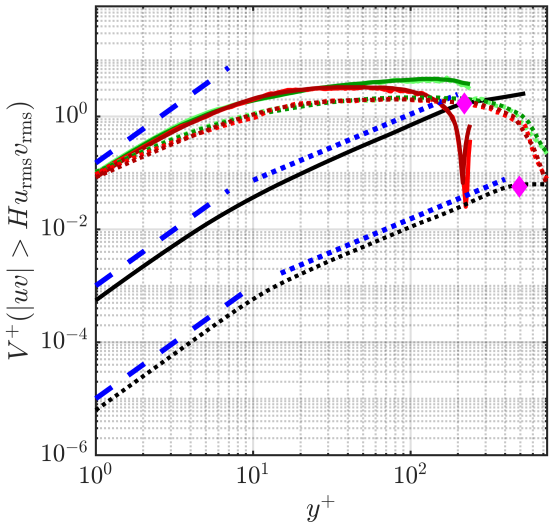

Figure 6. Inner-scaled conditional average of the wall-normal velocity component over intense uv, in log-log scale, for (solid lines) APG and (dotted lines) ZPG. Color code as in Fig. 5. The blue dashed and dotted lines are guides for the eye, for $V^+ \propto (y^+)^2$, and $V^+ \propto (y^+)^{1.17}$, respectively. The magenta diamonds indicate the locations of δ_{99}^D.

at the wall are constant (and equal to zero) in the streamwise and spanwise directions, the first derivative of V in the wall-normal direction vanishes, and therefore $V \propto (y^+)^2$ close to the wall [30]. In the buffer region, the scaling of V is not trivial to establish. In the present work, we limit ourselves to observe empirically that $V \propto (y^+)^{1.17}$. The same scaling seems to apply for both APG and ZPG, despite the difference of approximately one order of magnitude in value, but not to the conditional value of V over Reynolds-stress events.

The conditional average allows the comparison of intense events in the two cases, but does not give information about their relevance to determine the mean properties. Thus, we examine the probability of belonging to intense events and to each quadrant, and the fractional contribution to the mean V (Fig. 7). Note that the fractional contribution is defined as the conditional average weighted with the probability of occurrence. Remarkably, the probability of occurrence of intense events as a function of the wall-normal distance is similar in APG and ZPG, and, in both cases, it varies between 6% and 9% through the turbulent region for $H = 2$. The most significant difference is observed in the relative proportion of ejections and sweeps in the buffer layer. Below $y^+ \simeq 10$, they are in good agreement in both cases, and sweeps are more common than ejections, which is a consequence of the short distance from the wall. In the ZPG TBL, at $y^+ \simeq 10$, ejections become more common than sweeps. On the other hand, in the APG TBL, sweeps remain more common than ejections up to a distance from the wall of $y^+ \simeq 80$. The fact that the probability of occurrence and the intensity of the events are both relatively similar in APG and ZPG, despite the significant difference in the values of the mean V, implies that the fractional contributions of intense events are less significant in APG than in ZPG, in particular where the wall-normal convection is stronger. In fact, the fractional contributions to V in the APG are well below the mean, even if only intense ejections are considered. This phenomenon is

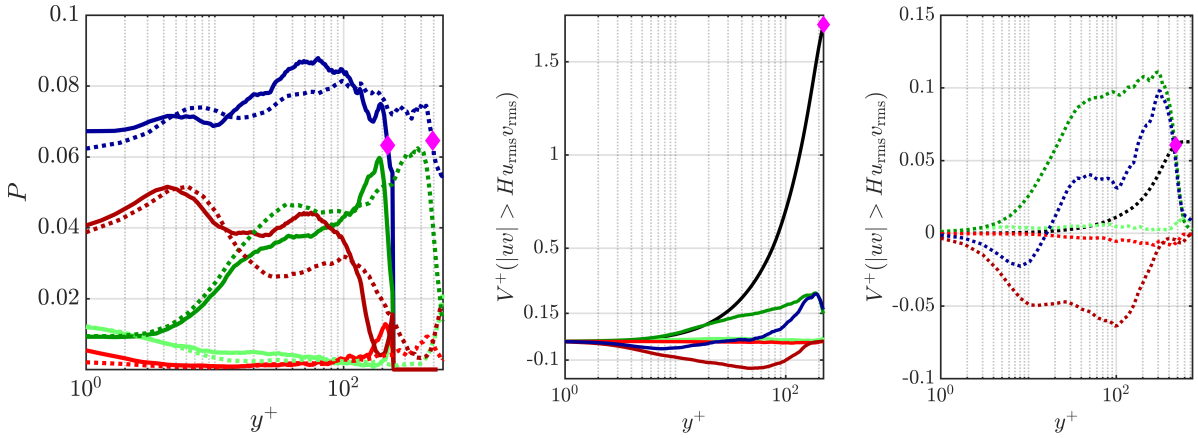

Figure 7. (Left) Probability of belonging to (blue lines) any intense uv event and (red and green lines) specific quadrants. (Middle and right) Fractional contribution to the wall-normal component of the velocity for (coloured lines) different quadrants compared with the mean (black lines) and the overall contribution of all intense events (blue lines). The colour code for different quadrant is the same as in Fig. 5. Solid and dotted lines are for APG and ZPG, respectively. The magenta diamonds indicate the locations of δ_{99}^D.

particularly evident at high wall-normal distances, where V is more than 10 times larger than in ZPG, and the fractional contribution from ejections is several times smaller than V. Moreover, since V conditioned at sweeps events has a similar order of magnitude but opposite sign, the combined contribution of the intense Reynolds-stress events is even lower. In ZPG, the relation between fractional contributions and mean velocity is virtually the opposite to that in APG. Except for the wake region, where few intense turbulent structures are detected, the fractional contributions from ejections is higher than V, as well as the modules of the contributions from sweeps, despite the fact that both of them both never account for more than 5% of the volume. Moreover, since sweeps are less common than ejections in the buffer region, but they have both the same intensity, the total contribution from intense events in ZPG is higher than the mean. Under this perspective, the results for ZPG are similar to what is observed in channel and duct flows [27]. In these cases, the fractional contributions to the vertical velocity, which is positive due to the predominance of ejections, is counterbalanced by the region of the domain not included in coherent structures. Lastly, in both APG and ZPG, the fractional contribution of inward and outward interactions is almost negligible, due to the low probability of occurrence of these events. This result suggests that the more intense wall-normal convection characteristic of APG TBLs is mainly a mean effect, which is not due to intense turbulent fluctuations. However, the actual intensity of the vertical fluctuations is increased significantly for the APG.

4. Conclusions

In the present study, we examined coherent structures in wall turbulence, defined as three-dimensional Reynolds-stress events, in the APG boundary layer developing over the suction side of a NACA4412 wing section at a chord Reynolds number of $Re_c = 200,000$ ($Re_\theta \simeq 1100$), and in a ZPG TBL at slightly higher Reynolds number ($Re_\theta \simeq 1200$). The structure-detection process follows the three-dimensional extension of the quadrant analysis introduced by Lozano-Durán *et al.* [8], and it is performed as a post-processing analysis on flow fields obtained as a result of high-fidelity numerical simulations. We focused on two different aspects, *i.e.* whether it is possible to apply the same structure-identification procedure as in internal turbulent flow,

and the contribution of the coherent structures to the mean wall-normal convection.

We observed that applying the condition usually employed in the quadrant analysis, *i.e.* $|uv| > Hu_{\rm rms}v_{\rm rms}$, yields the detection of very large structures in the non-turbulent region of the computational domain. These structures correspond to the fluctuations induced by the oscillation of the TNTI, and are not related to ejections or sweeps. They tend to be more persistent than the latter for increasing values of the threshold H, and much larger relative to the size of the domain. Consequently, the percolation analysis over the entire domain gives a result which is not in agreement with that in internal flows, such as turbulent channel and duct. However, we found that if the structure identification is performed in the turbulent region only, the agreement with internal flows is significantly improved. To identify the turbulent region of the domain, we employ three different criteria to define the TNTI, calibrated to give the same boundary-layer thickness on average, and we found that they provide similar results. Overall, our findings indicate that it is necessary to limit the structure identification to the turbulent region, through the use of a method to identify the TNTI.

To investigate the relation between pressure-gradient effects and intense uv, we examine the average of the vertical component of the velocity conditioned at the coherent structures belonging to each quadrant and their fractional contribution to the same quantity. In channel and duct flows, ejections are more frequent and more intense than sweeps, at least above the viscous sub-layer. Therefore, the fractional contribution to the velocity in the wall-normal direction from intense events is positive, and the contribution from less intense events counterbalances it. We observed that a similar scenario occurs in ZPG turbulent boundary layer, while APG are significantly different. In fact, in the latter, the fractional contribution of intense Reynolds-stress events is much lower than the mean wall-normal convection. Furthermore, in APG intense events are in general stronger than in ZPG and sweeps are relatively more common than ejections. These results suggest that, although the adverse pressure gradient has an impact on the turbulent fluctuations, the wall-normal convection is mainly a mean effect, rather than *e.g.* the results of either more frequent or stronger ejections.

Due to the exploratory nature of the present study, several aspects are left for future research. Concerning the region of the domain to perform the coherent-structure identification, the current procedure requires to determine *a priori* the boundary-layer thickness, δ_{99}^D, and to calibrate *ad hoc* parameters such as C_ω, C_k^f, and C_k^e. The sensitivity of the percolation analysis to the location of the TNTI suggests that it may be possible to define the turbulent region of the domain in terms of the percolation crisis. Such a connection would enable the formulation of a more general definition of the TNTI. The most promising direction for future research, however, is to investigate in more detail the relation between the pressure-gradient effects on the mean properties of the flow and those on coherent structures.

Acknowledgments

This study was funded by the Coturb program of the European Research Council, by the Swedish Foundation for Strategic Research (SSF), project "In-Situ Big Data Analysis for Flow and Climate Simulations" (ref. number BD15-0082), by the Knut and Alice Wallenberg (KAW) Foundation and by the Swedish Research Council (VR). The simulations were performed on resources provided by the Swedish National Infrastructure for Computing (SNIC) at PDC, KTH. We thank Callum Atkinson for helpful comments on the manuscript.

References

[1] P. R. Spalart and J. H. Watmuff. Experimental and numerical study of a turbulent boundary layer with pressure gradients. *J. Fluid Mech.*, 249:337–371, 1993.

[2] K. Jansen. Large-eddy simulation of flow around a NACA 4412 airfoil using unstructured grids. *CTR Annu. Res. Br.*, pages 225–232, 1996.

[3] H. Shan, L. Jiang, and C. Liu. Direct numerical simulation of flow separation around a NACA 0012 airfoil. *Comput. Fluids*, 34:1096–1114, 2005.
[4] S.M. Hosseini, R. Vinuesa, P. Schlatter, A. Hanifi, and D.S. Henningson. Direct numerical simulation of the flow around a wing section at moderate Reynolds number. *Int. J. Heat Fluid Flow*, 61:117–128, 2016.
[5] R. Vinuesa, P. S. Negi, M. Atzori, A. Hanifi, D. S. Henningson, and P. Schlatter. Turbulent boundary layers around wing sections up to $Re_c = 1,000,000$. *Int. J. Heat Fluid Flow*, 72:86–99, 2018.
[6] A. Bobke, R. Vinuesa, R. Örlü, and P. Schlatter. History effects and near equilibrium in adverse-pressure-gradient turbulent boundary layers. *J. Fluid Mech.*, 820:667–692, 2017.
[7] Wallace, J. M., Eckelman, H. and Brodkey, R. S. The wall region in turbulent shear flow. *J. Fluid Mech.*, 54:39–48, 1972.
[8] A. Lozano-Durán, O. Flores, and J. Jiménez. The three-dimensional structure of momentum transfer in turbulent channels. *J. Fluid Mech.*, 694:100–130, 2012.
[9] Y. Maciel, M. P. Simens, and A. G. Gungor. Coherent structures in a non-equilibrium large-velocity-defect turbulent boundary layer. *Flow Turbul. Combust.*, 98:1–20, 2016.
[10] A. Tanarro, R. Vinuesa, and P. Schlatter. Effect of adverse pressure gradients on turbulent wing boundary layers. *J. Fluid Mech.*, 883:A8, 2020.
[11] J. Jiménez, S. Hoyas, M.P. Simens, and Y. Mizuno. Turbulent boundary layers and channels at moderate Reynolds numbers. *J. Fluid Mech.*, 657:335–360, 2010.
[12] P. F. Fischer, J. W. Lottes, and S. G. Kerkemeier. Available at: `http://nek5000.mcs.anl.gov`, 2008.
[13] P. Schlatter, S. Stolz, and L. Kleiser. Les of transitional flows using the approximate deconvolution model. *Int. J. Heat Fluid Flow*, 25:549–558, 2004.
[14] P. Schlatter and R. Örlü. Turbulent boundary layers at moderate reynolds numbers, inflow length and tripping effects. *J. Fluid Mech.*, 710:5–34, 2012.
[15] F.R. Menter. Two-equation eddy-viscosity turbulence models for engineering applications. *AIAA J.*, 32:1598–1605, 1994.
[16] S. Dong, G.E. Karniadakis, and C. Chryssostomidis. A robust and accurate outflow boundary condition for incompressible flow simulations on severely-truncated unbounded domains. *J. Comput. Phys.*, 261:83–105, 2014.
[17] M.P. Simens, J. Jiménez, S. Hoyas, and Y. Mizuno. A high-resolution code for turbulent boundary layers. *J. Comput. Phys.*, 228:4218–4231, 2009.
[18] M. Atzori, R. Vinuesa, A. Stroh, B. Frohnapfel, and P. Schlatter. ETMM-12. arXiv:1812.03762, 2018.
[19] Y.S. Kwon, N. Hutchins, and J.P. Monty. On the use of the Reynolds decomposition in the intermitten region of turbulent boundary layers. *J. Fluid Mech.*, 794:5–16, 2016.
[20] J. Hwang and H.J. Sung. Wall-attached structures of velocity fluctuations in a turbulent boundary layer. *J. Fluid Mech.*, 856:958–983, 2018.
[21] D.K. Bisset, J.C.R. Hunt, and M.M. Rogers. The turbulent/non-turbulent interface bounding a far wake. *J. Fluid Mech.*, 451:383–410, 2002.
[22] K. Chauhan, J. Philip, C. M. de Silva, N. Hutchins, and I. Marusic. The turbulent/non-turbulent interface and entrainment in a boundary layer. *J. Fluid Mech.*, 742:119–151, 2014.
[23] P. H. Alfredsson, A Segalini, and R. Örlü. A new scaling for the streamwise turbulence intensity in wall-bounded turbulent flows and what it tells us about the "outer" peak. *Phys. Fluids*, 23:041702, 2011.
[24] R. Vinuesa, A. Bobke, R. Örlü, and P. Schlatter. On determining characteristic length scales in pressure-gradient turbulent boundary layers. *Phys. Fluids*, 27:105107, 2016.
[25] K.A. Chauhan, P.A. Monkewitz, and H.M. Nagib. Inner scaling for wall-bounded flows subject to large pressure gradients. *Fluid Dyn. Res.*, 41:021404, 2009.
[26] T.B. Nickels. Inner scaling for wall-bounded flows subject to large pressure gradients. *J. Fluid Mech.*, 521:217–239, 2004.
[27] M. Atzori, R. Vinuesa, A. Lozano-Durán, and P. Schlatter. Characterization of turbulent coherent structures in square duct flow. *J. Phys.: Conf. Ser.*, 1001:012008, 2018.
[28] F. Moisy and J. Jiménez. Geometry and clustering of intense structures in isotropic turbulence. *J. Fluid Mech.*, 513:111–133, 2004.
[29] K. Christensen and N. R. Moloney. *Complexity and Criticality*. Imperial College Press, Advanced Physics Texts, London, United Kingdom, 2005.
[30] P.A. Monkewitz and H. M. Nagib. Large-Reynolds-number asymptotics of the streamwise normal stress in zero-pressure-gradient turbulent boundary layers. *J. Fluid Mech.*, 783:474–503, 2015.